

Application of Hyperspectral LiDAR on 3-D Chlorophyll-Nitrogen Mapping of *Rohdea Japonica* in Laboratory

Lin Du¹, Zhili Jin, Bowen Chen, Biwu Chen¹, Wei Gao¹, Jian Yang, Shuo Shi¹, Member, IEEE, Shalei Song¹, Mengmeng Wang¹, Wei Gong¹, and Wei Wang¹

Abstract—Biochemicals, such as chlorophyll (Chl) and nitrogen (N), are closely related to photosynthesis process of vegetation. Their accurate estimation is an important topic in remote sensing of vegetation. Previous studies mainly focused on Chl-N content inversion in leaf and canopy level, and few cared about their 3-D distributions, which was also an important indicator for the growth status of vegetation (GSV). Hyperspectral LiDAR (HSL) is a novel active remote sensing technology, which has target-sensitive band with hyperspectra resolution. Its 3-D point cloud data simultaneously contains rich spectral and precise geometrical characteristics of the target. This work aims to apply HSL data on 3-D Chl-N content mapping in vegetation through constructing HSL-based spectral indices (SIs). Except for following the SI forms of previous works, the normalized differential vegetation index and ratio index (RI) with four broadbands in an HSL spectral space were successively proposed to invert Chl-N content for the whole vegetation based on the artificial neural network (ANN) method. These four broadbands were transformed based on the relative spectral response curve of detector and the feature weights (FWs) of multiwavelength, respectively. Results show that most HSL-based ANN models can accurately invert Chl-N content with a mean R^2 of >0.75 , and some that fusing broadband data with convolution

Manuscript received February 5, 2021; revised July 24, 2021 and August 8, 2021; accepted September 7, 2021. Date of publication September 9, 2021; date of current version October 7, 2021. This work was supported in part by the National Key R&D Program of China under Grant 2018YFB0504500, in part by the National Natural Science Foundation of China under Grant 41971307, and in part by the Fundamental Research Funds for the Central Universities, China University of Geosciences (Wuhan) under Grant CUG170662. (Corresponding author: Wei Gao.)

Lin Du and Mengmeng Wang are with the Faculty of Information Engineering, School of Geography and Information Engineering, China University of Geosciences, Wuhan 430074, China, and also with the Artificial Intelligence School, Wuchang University of Technology, Wuhan 430223, China (e-mail: dulin@cug.edu.cn; wangmm@cug.edu.cn).

Wei Gao and Jian Yang are with the School of Geography and Information Engineering, China University of Geosciences, Wuhan 430074, China (e-mail: gaowei@cug.edu.cn; yangjian@cug.edu.cn).

Zhili Jin and Wei Wang are with the School of Geoscience and Info-Physics, Central South University, Changsha 410083, China (e-mail: jinzhili@csu.edu.cn; wangweicn@csu.edu.cn).

Bowen Chen, Biwu Chen, Shuo Shi, and Wei Gong are with the State Key Laboratory of Information Engineering in Surveying, Mapping and Remote Sensing, Wuhan University, Wuhan 430079, China (e-mail: chenbowen1204@whu.edu.cn; cbw_think@whu.edu.cn; shishuo@whu.edu.cn; weigong@whu.edu.cn).

Shalei Song is with the State Key Laboratory of Magnetic Resonance and Atomic and Molecular Physics, Wuhan Institute of Physics and Mathematics, Chinese Academy of Sciences, Wuhan 430071, China (e-mail: songshalei@gmail.com).

This article has supplementary downloadable material available at <https://doi.org/10.1109/JSTARS.2021.3111295>, provided by the authors.

Digital Object Identifier 10.1109/JSTARS.2021.3111295

transformation, namely the FW-based RI, can even obtain a model R^2 of 0.84 for N content inversion. Thus, HSL can be efficiently applied to 3-D Chl-N content mapping of vegetation and has great potential in GSV monitoring.

Index Terms—Artificial neural network (ANN), broadband spectral index, Chl-N content mapping, hyperspectral LiDAR (HSL).

I. INTRODUCTION

CHLOROPHYLL and nitrogen (Chl-N) contents are significant indicators for photosynthetic process of vegetation, which is closely related to the status of vegetation growth (GSV) [1]. Therefore, accurate estimation of Chl-N content is an important topic in vegetation research. Remote sensing method, including passive hyperspectral images and active LiDAR, is an efficient and nondestructive technology for Chl-N content estimation in vegetation, and it has been widely applied in many research works [2]–[4]. Passive remote sensing images are sensitive to solar illumination and atmosphere condition, but being insensitive to the changes among vegetation elements, such as the leaves and branches [5]. Additionally, the soil background and canopy geometry of vegetation can confound the spectral echoes of foliage, which cannot be clearly distinguished by passive 2-D images [6], [7]. As an active remote sensing technology, LiDAR is independent from solar illumination and can separate soil background noise by obtaining vertical information of vegetation [8]. At leaf scale, Magney *et al.* [9] conducted a terrestrial laser scanner (TLS) to assess the suitability of green laser return intensity (GLRI, 532 nm) in understanding the leaf photoprotective mechanisms. They found that the relationship between photoprotective nonphotochemical quenching and GLRI for individual leaves exhibited a coefficient of determination (R^2) of 0.52 (wheat) to 0.78 (sunflower), and they stated that the GLRI-based TLS had great prospects in ascertaining foliar 3-D physiological information. At plant scale, Zhu *et al.* [10] used a near-infrared (NIR, 1550 nm) TLS for leaf water mapping, and successfully obtained its 3-D distribution of *Polyscias fabian* and *Camellia japonica* based on the backscatter intensity of TLS. Eitel *et al.* [11] used a GLRI-based TLS to measure N nutrition index for wheat in tillering and jointing stages, and they demonstrated that TLS could provide useful information for improving N management during early season growth.

Generally, the 3-D distribution of Chl content or leaf nitrogen content (LNC) from top to bottom is the healthy map of a plant, which can be used to evaluate the biomass accumulation capacity of different vegetation leaves, then to provide the necessary guide for agriculture and forestry activities, such as the fertilization and irrigation management [12], [13]. Thus, it is necessary and efficient to combine the spectral properties and 3-D physiological information of vegetation sufficiently [14], [15]. In practice, fusing passive 2-D images and LiDAR data has achieved some satisfied results [16]. However, datasets from two instruments needed to be registered in spatial and temporal, which makes it complex in field practice [17]. To reduce this restriction, Eitel *et al.* [18] tried and designed a tractor-mountable LiDAR with two lasers, green (532 nm) and red (658 nm) to improve laser-based estimation of LNC by calculating laser spectral indices (SIs) based on the ratio of GLRI and red laser return intensity. Following the similar idea, the hyperspectral LiDAR (HSL) with an active emitted laser in multiwavelength has shown great potential in vegetation monitoring because of its outstanding advantage of obtaining rich spectral properties of the target [19], [20].

The HSL system consists of a supercontinuum laser and a multichannel detector, thus can accurately obtain 3-D point cloud data of vegetation, which simultaneously contain rich spectral and precise geometric characteristics [21]. These characteristics are significantly important features reflecting vegetation physical properties [22]. HSL owns numerous biochemical-sensitive wavelengths, which makes it possible to construct more efficient HSL-based SIs for 3-D Chl-N content mapping of vegetation, therefore giving a macroscopic glance of the GSV. Hakala *et al.* [23] presented a novel 16-wavelength HSL system and then produced 3-D point cloud data of Norway spruce (*Picea abies*) with the reflectance intensity and some HSL-based SI. Li *et al.* [24] indicated that the leaf biochemical contents, including nitrogen (N), Chl a/b, and carotenoid (Car), are closely related to these HSL-based SIs at short visible wavelength. Thereafter, Nevalainen *et al.* [17], [25] analyzed the potential of an eight-wavelength HSL in Chl-N content estimation based on some HSL-based SIs, including the chlorophyll absorption ratio index (CARI), modified simple ratio. Du *et al.* [19] used an HSL system with 32-wavelength to estimate rice LNC, and successfully classified rice leaf samples under different nitrogen fertilizations through support vector machine. Successively, they estimated rice LNC by proposing some HSL-based SIs, and found two integral SIs with proper integral limits, namely the normalized area over reflectance curve (NAOC) and reflectance integral index, performed better in LNC inversion than the other SIs in special narrow band [26]. However, these studies mainly focused on applying HSL on N content estimation of vegetation in leaf level, and rarely obtained 3-D N map for the entire plant.

The vegetation-sensitive SIs are commonly defined as the combination of reflectance in NIR and visible range with specific narrow band [27]–[29], or some being formed with a vague broadband, such as the normalized differential vegetation index (NDVI) and ratio index (RI), which are calculated using NIR and red band. The broadband SIs are usually sensitive to more different vegetation types and have been widely applied in many fields. For instance, the NDVI products of moderate resolution imaging spectroradiometer (MODIS) have been applied in vegetation

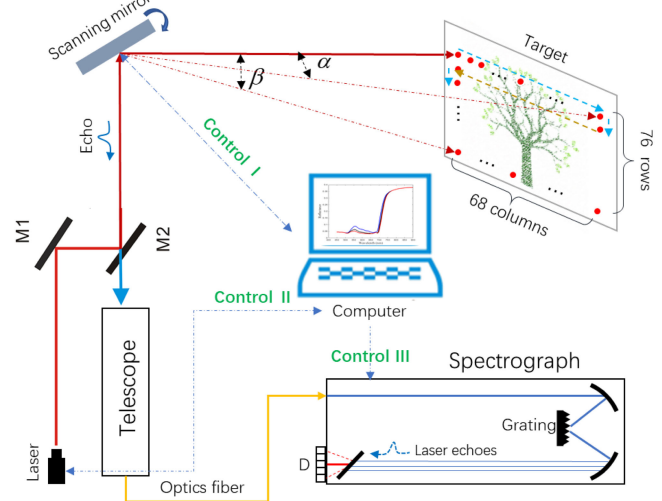


Fig. 1. HSL system used for vegetation scanning. The target was placed away from the scanning mirror in 5.6 m and being scanned by the laser spot in a “S-route” with two angles, namely α and β in horizontal and vertical directions, respectively.

dynamics monitoring [30], land cover change detection [31], and crop yield forecasting [32]. Moreover, a good performance of NAOC on LNC estimation in the study of Nevalainen *et al.* [25] can also support this judgment to some extent. Elvidge and Chen [33] compared the performance of broad- and narrowband SIs in leaf area index and percent green cover estimation, they stated that broadband SIs could further reduce the background effects on parameter inversion, which persisted in narrowband SIs. The broadband SIs are conducted by convolving narrowband spectra with the relative spectral response (RSR) curve of a high spectra-resolution detector, such as the Analytical Spectral Devices, Inc. (ASD, Boulder, CO, USA) [34]. Like the passive remote sensing method, HSL-based SIs in broadband can be convolved using the RSR of a multichannel APD detector and the HSL spectral data, by which more feature wavelengths of HSL can be fused to construct the spectral-space SIs for Chl-N content inversion.

Following the aforementioned exposition, this work aimed to apply HSL data on 3-D Chl-N content mapping in vegetation. Specifically, we aimed to construct HSL-based SIs following previous work, and then transform the multiwavelength spectra of HSL into a four broadband spectral space, in which NDVI and RI were derived for Chl-N content mapping. These four broadbands were transformed through RSR-convolution based on the HSL wavelengths ranging from 436 to 808 nm. As a comparison, another broadband transformation method, namely, feature weights (FWs) were utilized simultaneously.

II. INSTRUMENT

The HSL system used for vegetation scanning in this study worked with five fundamental components basically, including the laser emission, target scanning, photovoltaic receiving and conversion, data processing, and system control (see Fig. 1). The emitted laser passed through a high reflectance mirror (M1) and reached to another mirror (M2, diameter = 50.8 mm), which had the approximate size as the secondary mirror of a telescope. In

this way, the laser was coaxial with the optical axis of telescope and then illuminated the target perpendicularly through the scanning mirror. The scanning mirror was coated with total reflective material, which could enhance the echo signal as an extension of the telescope's field of view. The echoes reflected from the target surface were polychromatic, which could be collected with an achromatic telescope and then be focused into a grating spectrograph through optics fiber for multispectra separation. Finally, the separated optical echoes were converted to voltage value with an APD array detector (see D in Fig. 1). The control section worked simultaneously to trigger the process of data collecting and scanning mirror rotation when the emitted laser gave a "start pulse" to the computer. This control mechanism was processed through controls I, II, and III in Fig. 1.

The emitted laser was generated with a supercontinuum laser source from NKT photonics, which had an average output power of 100 mW, a pulse repetition rate of 20–24 kHz, 1–2 ns pulselwidth, and a spectrum with white light of 450–2400 nm. The telescope had a focal length of 400 mm and a diameter of 200 mm. The spectrograph was Czerny–Turner and worked with a blazed grating, which had a center wavelength of 500 nm and a groove of 150/mm. This grating had >50% spectral efficiency and 13.07-nm spectral resolution in the range of 400–800 nm. The APD array consisted of 32 discrete channels with a sensitive spectral range of 300–920 nm. In this study, the spectra for each point from the scene were discrete in 32 wavelengths ranging from 436 to 808 nm with a spectral resolution of 12 nm. More details about this HSL system have been introduced in the study of Nevalainen *et al.* [17]. The maximum distance between the laser spot emitted from the scanning mirror and the target is 5.6 m and its footprint size is about 1.5 cm at this position.

III. METHODS

A. Experiment Design and Data Measurement

Vegetation used in this study is *Rohdea japonica* (*R. japonica*), it belongs to *Dieffenbachia*, which is one species of *Araceae* [35]. It has a wide leaf where distributes obvious green areas in different degrees (see Fig. 2), which makes it clearly distinguished on the Chl content map. Theoretically, deeper degree of green color, higher Chl content on the edge of plant leaf. Because of the approximate linear relationship between Chl and N content, there distributes higher N content on the edge of plant leaf as well [19]. The plant was potted in a white porcelain basin and set onto a lifting platform. The white laser spot was located on the upper-left of a black cardboard (BC), which was considered as the background for the experimental scene. In order to make the BC position be fixed, a Plumbum lump was leaned against its downside closely.

HSL laser emitted through a scanning mirror and then illuminated the target with a perpendicular angle at the first point on BC. Being derived by electrical machinery of scanning mirror, the laser spot moved along a horizontal line first until reaching the right-most sides of target, then transformed once to the vertical direction and repeated back-visit scanning. During the "S-route" scanning, the angle could change with a constant that was determined by scanning interval in horizontal and vertical directions. In this way, there were 5168 points (76 × 68) located on the whole experiment scene obtained by HSL. Spectra



Fig. 2. Picture of the *R. japonica* used in this study. The pot was set onto a lifting platform whose height could be adjusted along the emitted laser position of the HSL system.

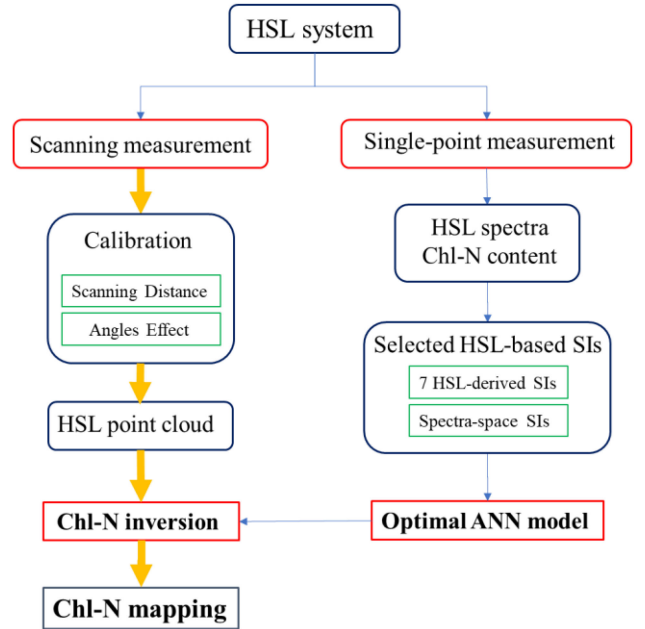


Fig. 3. Flowchart of the method for Chl-N mapping based on HSL point cloud data.

in 32 wavelengths and distance in 3-D space were collected simultaneously for each point.

Fig. 3 shows the method overview of this study: first, designing a single-point detection experiment to calibrate the scanning distance-angle effect with changing the distance-angle intervals; the incident angle calibration was conducted by calculating a dot product between the incident light and the normal vector of each point on *R. japonica* leaf. Successively, an independent measurement was conducted to obtain 109 single points on *R. japonica* leaf with HSL spectra and reference Chl-N content. These 109 samples were used to train and establish the Chl-N content inversion model with artificial neural network (ANN)

method. These 109 single points were selected on *R. japonica* plant randomly and discretely to ensure that the measured reference Chl-N content and HSL spectra were descriptive enough for the whole vegetation. They were located in a 76×68 point-matrix and their locations on the whole scanning scene were showed in supplementary Table I. Finally, selecting a series of HSL-derived SIs, including that based on the previous works and the four broadband NDVIs/RIs derived through the RSR- and FW- convolution transformation, to map 3-D distribution of Chl-N content based on the optimal ANN model. The reference Chl-N content of these samples was described in milligrams per gram based on SPAD value, which was the function of the measured transmission ratio in red (650 nm) and NIR (940 nm) band [36]. The SPAD values or SPAD-based indices have a linear or nonlinear relationship with Chl-N content [36]–[38], which is affected by many factors, such as the leaf features, plant species, and environmental light [39]. Some researchers stated that different crops shared a common relationship between SPAD and Chl content under the standard measurement conditions [40]. In present study, we obtained SPAD readings under controlled condition in a dark laboratory, and being measured in three times at the same position for one point, then averaging these three repetitions to obtain the reference Chl-N content for each sample.

B. ANN Model

The typical feed forward ANN model was used in present study to invert Chl-N content of vegetation. This type of ANN model comprises three layers: one input layer, one hidden layer, and one output layer. Each layer may include one or more neurons. Ten input neurons were used in present study, each representing a spectral variable. The input is a sum of all input variables X_i in (1), which can relate to their associated weights a_i . The output layer comprises one neuron, indicating the value of Chl-N content. A nonlinear activation function f_{non} could process an iteration to obtain an optimal output y (Chl-N content). The logarithmic (for the hidden and output layer neurons) transfer function has been implemented to fit nonlinear relationships between spectral variables and Chl-N content. There were 109 single points with reference Chl-N content and multiwavelength spectra were considered as the training and validation samples for ANN model establishment. During the “training” process, parameters a_i (network weights) and b_i (biases) were adjusted along with the gradient-decreased mean square error (MSE) until generating an optimum Chl-N value (y). Four commonly used training functions were conducted to update a_i and b_i , namely, Levenberg–Marquardt (LM) algorithm, Bayesian regularization (BR) algorithm, quasi-Newton (BFG) algorithm, and one step secant (OSS) algorithm. The validation process of ANN model was conducted with a k -fold cross-validation. In practice, typical range of k is 5–10: $k < 5$ might cause an issue and $k > 10$ need high computational cost because of the large number of training instances in each iteration while the small number of instances in a fold [41], [42]. Thus, samples in this study were split into five folds, four-fifths for training and one-fifth for validation. Repeating this cross-validation procedure five times until every fold has been used exactly once for validation. This iteration process performed with some controlled conditions, including

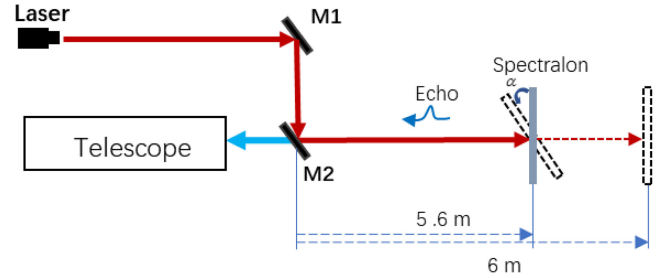


Fig. 4. Single-point detection experiment with different detection distance and scanning angle.

the minimum MSE of 10^{-3} , minimum gradient of 10^{-6} , and maximum iterations (epochs) of 100, any them can trigger the iteration process stopping. More details about ANN method can be found in the book of Yegnanarayana [43] and the documents of software MATLAB 2014b

$$y = f_{\text{non}} \left(\sum_{i=1}^n a_i X_i + b_i \right). \quad (1)$$

Based on the aforementioned optimizing process, some optimal ANN models with high R^2 for Chl-N content inversion were selected, and then be used for 3-D mapping of Chl-N content for the whole plant (5168 points) during the subsequent scanning experiment.

C. Distance-Angle Calibration

The incident angle and distance have significant influence on the backscatter intensity of HSL. Through radar range equation, incidence angle effect can be calibrated with a cosine function and distance can be calibrated with an empirical model, e.g., $1/R^2$ or $1/R^3$ [44]. However, these corrections are suitable for these perfect diffuse reflectors, whereas not always valid in many natural objects with complex surface properties. Some theoretical models are proposed to calibrate their effects on spectra intensity and usually being appropriate for numerous complex reflectors, e.g., Lommel–Seeliger law model [45], Phong model [46], Lambertian model, and Beckmann law model [47]. These models are combined with a physical model, namely bidirectional reflectance distribution function (BRDF), and needing some surface parameters, such as the roughness and grain size, which are usually difficult to obtain accurately. Moreover, BRDF cannot be measured because it is the ratio of infinitesimal quantities [44], [48]. Thus, the calibration of distance-angle effect in this study was conducted through designing a single-point detection experiment with a white panel (10×10 cm, $>99\%$ reflectance, Spectralon, Labsphere, Inc., North Sutton, NH, USA) (see Fig. 4). The Spectralon performed high diffuse reflectivity over the ultraviolet, visible, and NIR regions of the spectrum, which are commonly used to obtain target reflectance [49]. With a fixed distance, such as 5.6 m, reference reflectance with this Spectralon was utilized to explore the relationship between HSL spectral intensity and the scanning angle ranging from 0° to 70° . By placing the Spectralon at the ascending distance ranging from 5.6 to 6.0 m with an average interval of 0.02 m, laser echoes were successively collected by HSL system. In this way, the effect of distance and scanning angle on spectral intensity of HSL can be

finally calibrated by the special fitting functions. Successively, a normal vector for each scanning point on *R. japonica* leaf was calculated and then obtained its corresponding incidence angle μ based on the dot product between the normal vector and incidence light. Finally, calibrating the effect of incidence angle on the HSL signal using (2), in which $R_{\text{Dis-Calibrated}}$ was the signal calibrated with distance factor and $R_{\text{Calibrated}}$ was the calibrated HSL intensity by the distance and angle factors. Some researchers reported that an overcorrection might happen when the incidence angle is beyond a threshold [50], [51]. We have conducted the intensity-incidence angle experiments with different systems, including the multispectral LiDAR with four bands, HSL, and ASD, and we found that the Spectralon intensity for an incidence angle larger than 60° is difficult to analyze its effect on reflectance intensity. Thus, we set the angle threshold as 60° for the incidence angle calibration in this study during the scanning experiment. Hu *et al.* [52] conducted the similar experiments on different leaves from 0° to 80° and they found that the specular reflection was significant in red band, and its non-Lambertian characteristics are obvious. However, the reflectance characteristic in NIR band followed the Lambert-scattering law, but little specular reflection was observed. In this study, we analyzed the angle effect of three single wavelengths (472, 532, and 736 nm) and three broadbands (B1, B2, and B4) on reflectance characteristics of white panel, then to obtain the pure reflectance formula for 3-D vegetation scanning

$$R_{\text{calibrated}} = \begin{cases} \frac{R_{\text{Dis-calibrated}}}{\cos(\mu)}, & \mu < 60^\circ \\ \frac{R_{\text{Dis-calibrated}}}{\cos(60)}, & \mu \geq 60^\circ \end{cases}. \quad (2)$$

D. HSL-Based SIs

There are lots of SIs that can be used for Chl-N content invention based on the 32-channel HSL spectra, such as the previous works [19], [26]. However, some of them did not perform well combining with ANN method. Through a repetitive process of selection and optimizing with ANN iterations, seven optimal SIs with high R^2 (such as >0.6) were sorted and then used to invert Chl-N content (see Table I) in this study. These seven HSL-based SIs were formed with central wavelength of each discrete channel of HSL and were calculated with more than two wavelengths, such as CARI1 [53], CARI2 [54], modified triangular vegetation index (MTVI) [55], and red-edge vegetation stress index (RVSI) [56], as well as an integral index, called NAOC, which was a sum of the reflectance in wavelength located in 600–800 nm [57]. Besides, there were some SIs combined feature wavelengths in a nonlinear form, such as the optimal vegetation index (VIopt) [58], CARI2, and nonlinear vegetation index (NLVI) [59].

E. Broadband SIs in HSL Spectral Space

Multiwavelength is one of the advantages of HSL in obtaining more richer spectral characteristics of the target than the other active remote sensing technology. In this study, HSL can collect laser echoes from the target with up to 32 discrete wavelengths. To fully utilize these feature wavelengths and to compare them with some NDVI products of spaceborne sensor, such as MODIS, which calculated NDVI values with band1

TABLE I
SIS DERIVED FROM HSL SPECTRA DATA FOR CHL-N MAPPING IN THIS STUDY

Spectral index	Formula	Reference
Optimal Vegetation Index (VIopt)	$(1+0.45) \times [(R800)^2 + 1] / (R670 + 0.45)$	Reyniers et al. (2006)
Chlorophyll Absorption Reflectance Index1(CARI1)	$(R700 - R670) - 0.2 \times (R700 + R550)$	Kim et al. (1994)
Chlorophyll Absorption Reflectance Index2(CARI2)	$(R700/R670) \times \text{sqrt}[(670 \times a + R670 + b)^2/(a^2 + 1)]$ $a = (R700 - R550)/150$ $b = R550 - 550 \times a$	Broge et al. (2001)
Modified Triangular Vegetation Index1(MTVI1)	$1.2 \times [1.2 \times (R800 - R550) - 2.5 \times (R670 - R550)]$	Haboudane et al. (2004)
Red-edge Vegetation Stress Index (RVSI)	$(R712 + R752)/2 - R732$	Merton et al. (1999)
Non-Linear Vegetation Index (NLVI) ^a	$(R_{\text{NIR}}^2 - R_R) / (R_{\text{NIR}}^2 + R_R)$	Goel et al. (1994)
Normalized Area Over Reflectance Curve (NAOC)*	$1 - \frac{\int_a^b R_\lambda d\lambda}{R(b-a)_{\max}}$	Delegido et al. (2010)

Note: ^a $R_{\text{NIR}} = 800 \text{ nm}$, $R_R = 670 \text{ nm}$; ^{*} R_λ and R_a are the reflectance at wavelength λ and a ; R_{\max} is the maximum far-red reflectance corresponding to reflectance at wavelength b . And a and b are the integral limits.

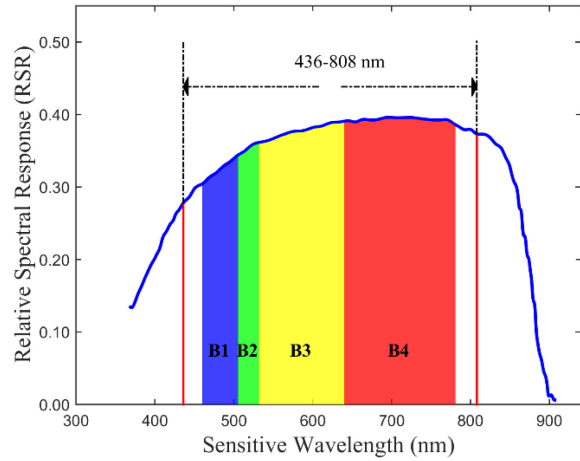


Fig. 5. RSR of the APD array and the sensitive bands for HSL system.

(620–670 nm) and band2 (841–876 nm), we transformed HSL multispectral band into four broadbands (see Fig. 5) using a convolution operation, namely, B1 (460–505 nm, blue), B2 (511–532 nm, green), B3 (538–640 nm, yellow), and B4 (646–780 nm, red), rather than calculating SIs by merely combining a single wavelength in narrowband. Because most Chl-sensitive bands usually located in green and red ranges, NDVI and RI values with B2 and B4 in HSL spectral space were calculated to model Chl-N content and then obtained their 3-D map through the optimal ANN model

$$\text{NDVI} = \frac{B4 - B2}{B4 + B2}, \text{RI} = \frac{B2}{B4}. \quad (3)$$

F. Convolution Transformation With HSL Bands

The convolution transformation with multiwavelength in this study was proposed based on the operation in (4), where $g(\lambda')$ was the vegetation reflectance obtained by HSL, $g(\lambda)$ was the

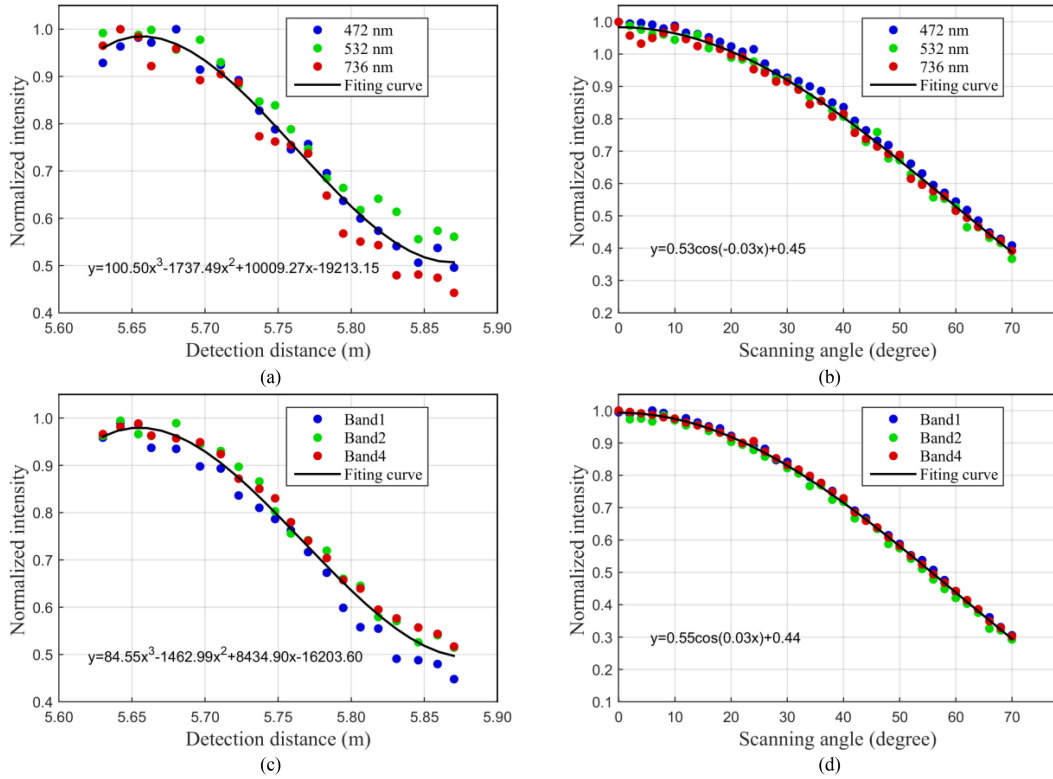


Fig. 6. Distance-angle factor calibration for HSL, which was, respectively, carried out in three (a), (b) single bands and (c), (d) broadbands. The three-order polynomial function was used for distance fitting and cosine function for scanning angle.

function of wavelength and defined by two means. One was the RSR of photonic-sensitive detector, the other was the FWs of each feature band. The RSR is a fixed function of λ , in this study, it was determined by the sensitive band of an APD array ranging from 300 to 900 nm, which covered detection wavelength of HSL system completely (see Fig. 5). The FW indicated the contribution or sensitivity of each band to vegetation biochemicals of interest, and it was calculated based on the divergence value of each class divided according to vegetation species and biochemical contents, further details about the calculation process of FWs could be found in the study of Huang and He [60].

$$R_c = \sum_{\lambda_1}^{\lambda_2} f(\lambda) g(\lambda'). \quad (4)$$

IV. RESULTS

With distance-angle calibration (see Section IV-A), the 32-wavelength HSL was applied to map 3-D Chl-N distribution of vegetation, during which two types of HSL-based SIs were derived to model Chl-N content for each point. These types were seven commonly used SIs in previous work (see Section IV-B) and the broadband NDVI/RI in an HSL spectral space (see Section IV-C).

A. Calibration With Distance-Angle Factor

Three narrow bands covering blue (472 nm), green (532 nm), and red (736 nm) range were selected for point-cloud data calibration, and then being alternated with three derived broadbands

(B1, B2, and B4). For distance factor, we found that a three-order polynomial function could well fit HSL intensity at a distance range of 5.6–5.9 m [see Fig. 6(a) and (c)]. For the effect of scanning angle on HSL echo at each fixed distance, it could be calibrated with a cosine function by setting an angle resolution of 2° [see Fig. 6(b) and (d)].

After function fitting of distance and scanning angle, the effect of incidence angle on HSL signature was then calibrated with (2), and finally the whole vegetation scene was displayed in pseudocolor with three bands in Fig. 7. Compared with the original scene in Fig. 2, calibration process has improved some outliers. For example, the points in red (in red squares at the leaf edge) were corrected with green color in Fig. 7(a) and (b), and leaf color at vegetation bottom became intense. But we should notice that the displayed color of some points landed on white porcelain basin and Plumbum lump did not improve significantly, and even showed two different colors for the same target. Moreover, leaves displayed with three single bands [472, 532, and 736 nm in Fig. 7(b)] showed different green degrees with that using three spectral-space broadband [see Fig. 7(c) and (d)], which shared a similar color with real vegetation picture (see Fig. 2).

B. Chl-N Content Mapping With HSL-Derived SIs

Seven HSL-based SIs were used for biochemicals inversion based on the measured Chl-N content values (see Table II and supplementary Table I). The inversion model was ANN with four different training functions (see Table III), which have been introduced in Section III-A. The special training function did not

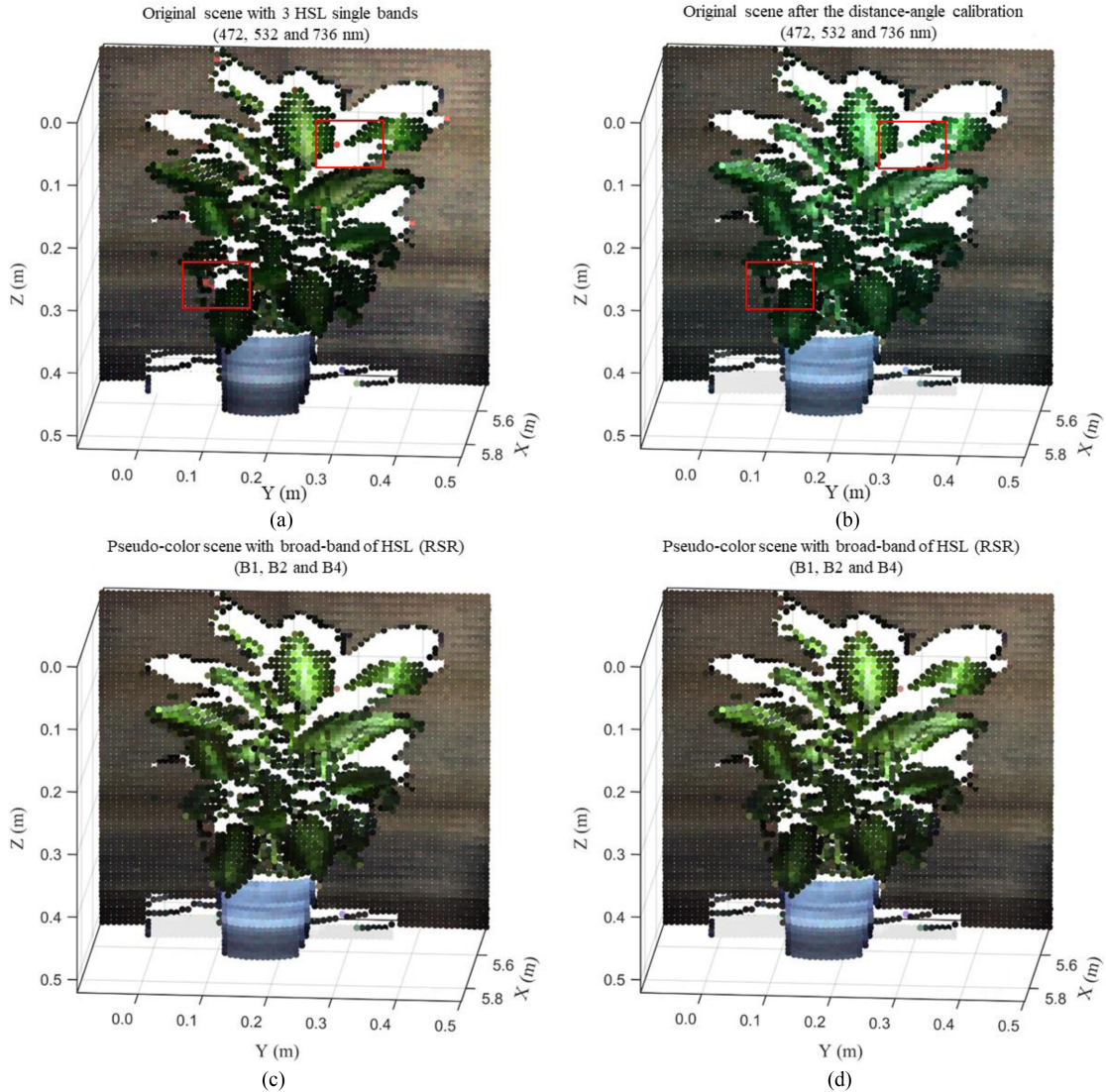


Fig. 7. Vegetation picture in pseudocolor with three bands. (a) Original HSL data in three single bands (472, 532, and 736 nm) and (b) calibrated with distance-angle factor. (c) and (d) Whole scene after distance-angle calibration in three RSR- and FW-based broadbands, respectively (B1, B2, and B4).

TABLE II
STATISTICAL FEATURES FOR CHL-N CONTENT IN SINGLE-POINT
MEASUREMENT

	Max-value	Min-value	Mean-value	Standard deviation
Chl (mg/g)	51.6	11	34.72	8.59
N (mg/g)	4.2	1.3	2.98	0.60

perform prior ability on Chl-N content inversion, whereas models with different SIs obtained distinct R^2 values. In particular, the NLVI-based ANN could optimize R^2 approximately to 0.83 for Chl content inversion. The other SIs could also achieve R^2 more than 0.75. For N content, the best ANN model was as high as three, which had R^2 of 0.8. The mean R^2 of these seven SI-based ANN models for Chl-N content inversion was 0.78 and 0.79, respectively [see Fig. 8(a) and (c)].

TABLE III
INVERSION RESULTS OF CHL-N CONTENT USING HSL-BASED SIS IN THIS
STUDY

		CARI1	CARI2	MTVI	RVSI	NAOC *	NLVI	Vlopt
Chl (mg/g)	R^2	0.76 ^{BFG}	0.76 ^{BFG}	0.78 ^{BR}	0.80 ^{BFG}	0.77 ^{BFG}	0.83 ^{LM}	0.75 ^{BFG}
	RMSE	3.62	3.75	4.09	3.31	3.78	2.94	5.97
N (mg/g)	R^2	0.76 ^{OSS}	0.80 ^{LM}	0.80 ^{OSS}	0.79 ^{LM}	0.80 ^{BFG}	0.77 ^{OSS}	0.78 ^{OSS}
	RMSE	0.30	0.26	0.28	0.25	0.26	0.27	0.29

Note: *The optimum integral limit for NAOC is 697 to 750 nm, which is selected based on its linear correlation coefficient with biochemical parameters. Details can be found in the study of Nevalainen *et al.* [17]. The superscripts of each R^2 value are four commonly used training functions, namely, LM algorithm, BR algorithm, BFG algorithm, and OSS algorithm.

In 3-D map [see Fig. 8(b) and (d)], we found that some leaves at vegetation bottom accumulated higher Chl-N content than the top leaves, and values for the same leaf was distributed from

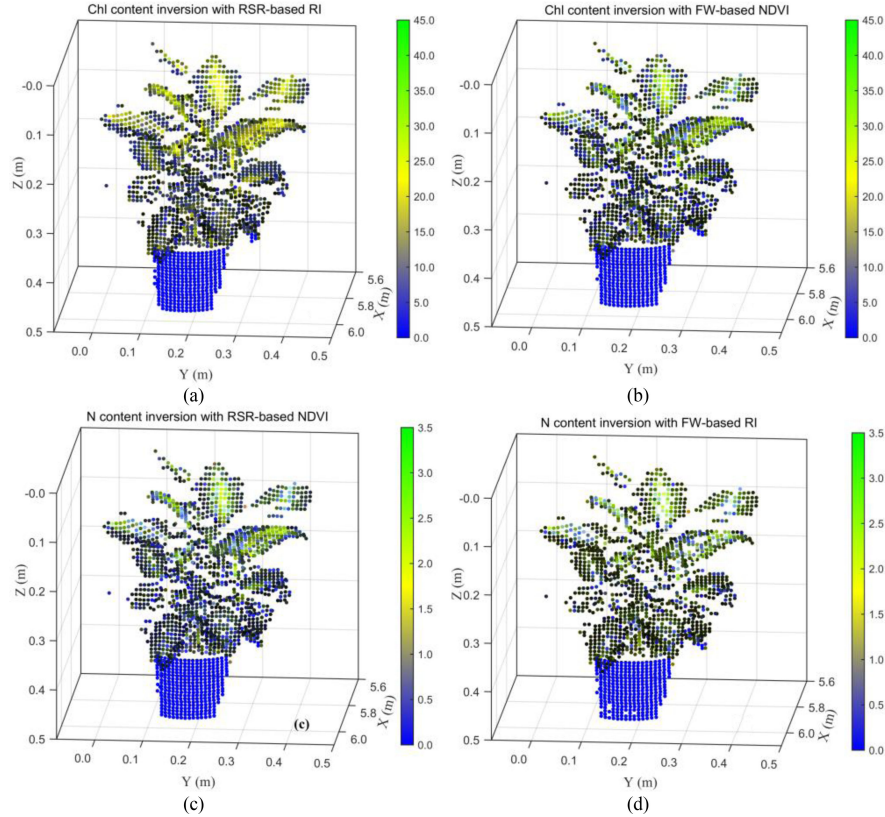


Fig. 8. (a) and (c), respectively, indicate the mean R^2 and RMSE values for Chl-N content inversion by using seven derived SIs from HSL data. (b) and (d) Chl-N mapping of *R. japonica* by using the optimal SI-based ANN models, namely NLVI for Chl and CARI2 for N.

TABLE IV
INVERSION RESULTS OF CHL-N CONTENT USING ANN METHOD WITH THE DERIVED BROADBAND SIS IN AN HSL SPECTRAL SPACE

	ANN with RSR-based broadband		ANN with FW-based broadband	
	NDVI	RI	NDVI	RI
Chl	R^2	0.76 ^{LM}	0.77 ^{LM}	0.81 ^{BFG}
(mg/g)	RMSE	3.74	4.18	2.05
N	R^2	0.78 ^{OSS}	0.75 ^{BFG}	0.79 ^{BFG}
(mg/g)	RMSE	0.17	0.16	0.18
				0.84 ^{BFG}
				0.13

foliage middle to the edge. However, there were some indisposed results in Chl-N map, some points on white porcelain basin were nonzero, and even showed equivalent Chl-N value to middle leaf (20–25 mg/g for Chl and 1.5–2 mg/g for N). This finding was consistent with the results in Fig. 7 where the white porcelain basin showed an unideal color.

C. Chl-N Content Mapping With Spectral Space SIs

Through the RSR- and FW-based convolution operation, 32 wavelengths of HSL were transformed into four broadbands (B1–4). B2 and B4 were used to derive NDVI and RI for Chl-N content inversion. With HSL-based broadband SIs, the model R^2 of Chl-N content inversion was more than 0.76, and some could even be improved up to 0.84 (FW-based SI for N content inversion in Table IV). Compared with the results in Table III, it could be found that the RMSE values for N inversion model with

spectral-space SIs were as low as half of that using HSL-derived SIs, which indicated that the convolution transmutation could efficiently improve the inversion of vegetative biochemicals. Meanwhile, we found that NDVI based on the optimal RSR- and FW-based broadband could distinguish vegetation leaf and white porcelain basin obviously with the inverted Chl-N contents close to 0 [dark blue color in Fig. 9(b) and (c)]. However, some points on white porcelain basin were still displayed with inseparable color in the vegetation top leaves, which meant that the broadband RI had the limited ability in Chl-N content inversion [see Fig. 9(a) and (d)].

V. DISCUSSION

A. Performance of HSL on 3-D Chl-N Mapping

HSL data have the advantage on biochemical content mapping in plant and leaf level, especially for Chl-N, which are highly sensitive to the spectral intensity in visible bands. In a plant, leaf maturity and translocation take place from upward to downward based on a multileaf zone divided by the leaf plastochnon index [61]. Leaves in top zone expand and import photosynthate, the middle zone leaves transport and convert biomass, and the bottom leaves transport primarily to lower stem and roots. Thus, the Chl-N content in photosynthetic apparatus of middle and bottom zone leaves is slightly higher than that in top zone [62]. Besides, the CO_2 assimilating amount of vegetation was commonly linearly correlated with the irradiation. However, the surplus energy will dissipate across the leaf lamina to avoid

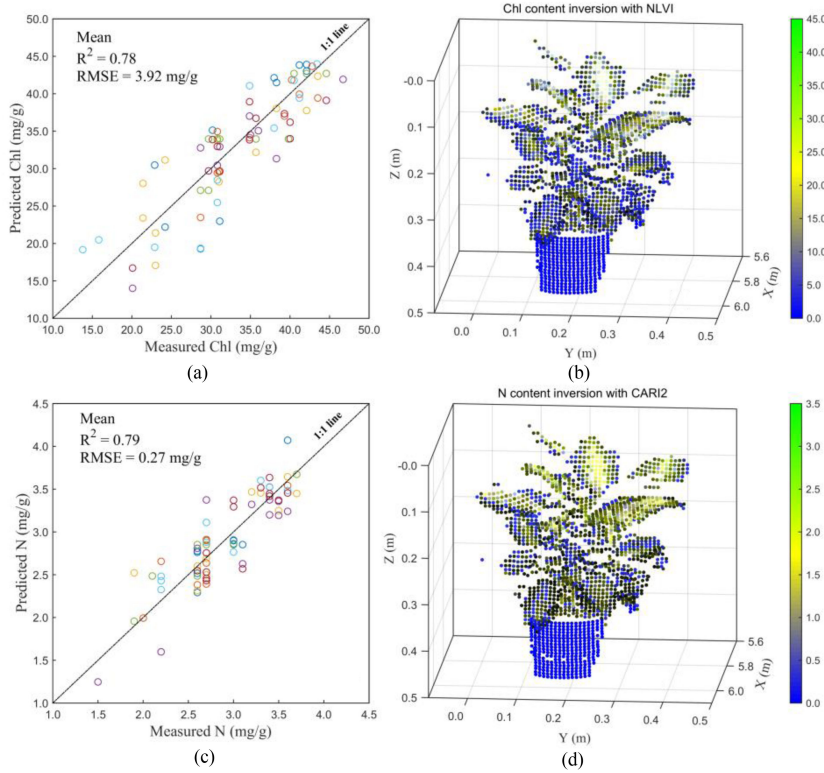


Fig. 9. Chl-N content mapping based on ANN model with the RSR- and FW-based broadband SIs. The RSR-based RI could be used to map (a) Chl content optimally while (c) NDVI for N. By using FW-based SIs, the optimal Chl content map was obtained with (b) NDVI while (d) RI for N.

an illumination damage when there are excess irradiation depending on the conversion of constituents of the xanthophyll cycle [9]. Thus, the leaves in top zone have an active photoprotective mechanism and lower Chl content. In shade, such as in the middle and bottom zones, leaves have lower irradiation but the higher Chl content and, thus, higher N content in light harvesting for an active photosynthesis process, which have been mapped with HSL in this study. In a leaf, the color is quite related to the type, proportion, and distribution of biochemical pigments. There are three kinds of pigment, including Chl (a and b), Car (lutein), and flavonoid pigment known as anthocyanin. Color of Chl is green, Car is orange-yellow, and anthocyanins are red or blue under acidic and alkaline conditions, respectively [63]. Because there is more Chl than Car, the leaves in common plant are always green. In this study, the mapped leaves showed obvious color gradient in green degree from leaf vein to edge, which means the biosynthesis process of Chl content in leaf center has been obstructed with some environment or genome factors [64], and the photosynthesis process in this part are not active enough. This botanical phenomenon has been observed by HSL system in this study, which could be a reliable technology to provide some informative data about the plant GSV in the future practice.

Xiao *et al.* [65] used an HSL system with a wavelength range of 409 to 914 nm to estimate the vertical Chl contents in maize, and obtained a series of optimal HSL-based SIs for Chl content inversion. In this study, seven selected SIs from 32 vegetation-sensitive wavelengths showed excellent performance on Chl-N content inversion based on ANN method. In the

previous work [26], we have used series of NDVI and RI in narrowband to fit rice N content, and have picked out some optimal narrowband combinations for Chl-N content inversion. However, these NDVI and RI had a R^2 of <0.6, which meant a poor inversion process. Thus, this study wanted to determine an efficient way to combine and integrate more features of HSL sensitive bands for vegetation Chl-N content estimation instead of applying all discrete spectral signature into the ANN model or the other method simply, such as the study of Yang *et al.* [66]. By convoluting feature wavelengths to derive HSL-based SIs in broadband, this study obtained R^2 of 0.84 and a low RMSE of 0.13 with the FW-based RI for N content inversion (see Table IV). Compared with the results using all bands with ANN method, which obtain a mean R^2 of 0.75 and a RMSE of 0.2, the N content inversion showed distinct improvement. Thus, convolution transformation based on the factors linking wavelength contribution to special biochemicals, such as the RSR and FW in this study, can be an efficient way to combine rich feature spectra of HSL for biochemicals mapping. Compared with obtaining 3-D distribution of SI values in vegetation rustically [25], [67], this study linked HSL data to the vegetation biochemicals further which could provide more information for GSV management and monitoring.

However, there are some indisposed results about this convolution transformation, such as the great improvement about Chl content inversion was not observed and the inversion process for some points landed on nonvegetation even obtained the equivalent Chl-N content to vegetation leaves. These findings indicated that the performance of HSL on 3-D Chl-N content

mapping greatly depends on the inversion accuracy of the ANN model, however, which is affected by many factors. These factors mainly include the experiment site and vegetation canopy structure, which are closely related to the GSV. Therefore, it is urgent to find a universal HSL-applicable model for vegetation biochemicals mapping so that HSL data can be widely used for vegetation monitoring in future works. Another reason for the unsatisfactory performance of white porcelain basin mapping may be that there were no single points located onto white porcelain basin, which meant that there was no reference Chl-N content that could be trained to optimize the ANN model for the white porcelain basin. Thus, future work needs a white reference panel integrated into the regular measurement to decrease some uncertainties during the measurement.

B. Limitation of the Inversion Method

In this study, Chl-N content inversion was conducted with ANN model, which input different HSL-based SIs, namely the ones in a form of previous work and the broadband NDVI/RI transformed by RSR and FW-based convolution. This inversion process is a black box for reader and the inner physical significant between biochemicals and the spectral intensity of HSL cannot be explained. Moreover, there are great correlations between each biochemical [67], which means that spectral changes in special bands are jointly determined by more than one biochemical content, thus the inversion model accuracy is greatly affected if one of them is separately considered as the ANN model input [68]. For example, Chl and Car contents are both sensitive with visible bands, so inverting Chl and Car content together can improve Chl content mapping with HSL data rather than inverting the Chl content without considering its correlations to Car.

Perhaps an inversion strategy based on the radiation transport model (RTM) is a good choice to take these aforementioned limitations into account during the biochemical inversion. The RTM, such as that used for vegetation research PROSAIL [69], or some specific RTMs for LiDAR characteristics simulation, including DART [70], RAPID [71], and GORT [72], usually worked with a physical process based on many inputs, including biochemicals (e.g., Chl, Car) and canopy structure parameters (e.g., leaf area index and leaf angle distribution). The RTM-based inversion process can be described clearly and the inversion strategy for each biochemical can be selected by a proper merit function of the RTM. However, N content is usually not the input for these RTMs, thus it is difficult to invert N content in physical model directly. Some indirect measured variables, such as the conversion efficiency of primary light energy or Chl content, are needed to transform N into the RTM, which makes it possible to analysis N content of vegetation correctly in a physical way [73].

Some proper SIs, especially those calculated with spectral ratio, can indeed decrease the effect of angle and distance on HSL spectral signals [72], [74]. Shi *et al.* [75] investigated the effect of incident angle on target measurement and found that the proposed LiDAR spectral ratio was insensitive to sensor-related factors, and the procedure of spectral ratio calibration could significantly improve the classification accuracy. We have investigated numerous SIs derived from HSL spectra and finally selected seven SIs in this study to invert the Chl-N content.

However, whether it is effective to compensate the effect of incidence angle on HSL signal by calculating these ratio SIs remains unknown. Perhaps, future work should compare the performance of SI deriving and function fitting on distance-angle factor calibration specially. Moreover, 109 single-point measurements were divided into two groups: 77 for training and calibration ANN model and 32 for the model validation. It seems sufficient for a regression model but not enough for the ANN model inversion. There were 5168 points scanned by HSL.

The SPAD-based method has been widely used in N status management [38], Chl content estimation [76], and grain yield assessment [77]. In present study, we measured SPAD values using Chl meter and then used these SPAD readings to derive the reference Chl-N content for ANN model establishment. However, the SPAD value is calculated with the transmittance in two wavelengths, namely 650 and 940 nm, which usually changed depending heavily on the Chl content within plant leaves. Thus, factors that can alter Chl content are also close related to the measured SPAD values, including irradiance condition, environment stress, and plant species [13], [39], [40]. Although the environmental conditions had been strictly controlled in a dark laboratory and the HSL measurement was conducted in hot pursuit after obtaining SPAD readings, there were some more works to calibrate SPAD readings with Chl-N content scrupulously.

C. Outlook

The HSL has the advantage of penetration into vegetation canopy. By scanning vegetation canopy from top to bottom or the opposite scanning direction, we can clearly explore its inner structure, such as the leaf area, tree branch distribution, and canopy size. These structural parameters result in great differences on the light use efficiency during the vegetation photosynthesis process, and accurate estimation of them is an important research field of remote sensing in vegetation. Thus, application of HSL data on 3-D vegetation detection should be explored further, especially on detecting its vertical canopy structure. The distribution density of leaf angle, one of canopy structure parameter, is highly related to the reflectance signals of HSL. Some relevant scholars have carried out preliminary exploration in the correction of factors, such as distance and incident angle [44], [49], [52], but the impact assessment and model correction of complex canopy reflection characteristics need to be further studied.

Biochemicals are usually closely related to biological variables, which are greatly predictable for the GSV, such as the biomass and yields. In this study, 3-D Chl-N content mapping obtained with HSL provided insight into the Chl-N distribution in vegetation. By combining the vertical structure of the canopy, total Chl-N content for the whole plant can be calculated to accurately monitor these significant biological variables in crops. Subsequently, the role of vegetation in ecosystem, or its ability of accumulating human-needed matters in agriculture, could be evaluated validly.

VI. CONCLUSION

It is an anticipated attempt to apply HSL on 3-D Chl-N content mapping in vegetation, and the results in this work have proved

that HSL is an efficient technology in mapping 3-D distribution of vegetation biochemicals. There were 32 feature wavelengths of HSL fused as numerous SIs for Chl-N content inversion, and we found some SI-based ANN models could obtain high correlations between spectral features and biochemicals. In particular, the RI-based ANN in broadband derived with FW-convolution could improve the inversion model R^2 to 0.84 for N content. By detecting the 3-D distribution of biochemicals from the top to bottom leaves in vegetation, we can evaluate the biomass and growth status of vegetation, even determine its contributions to the energy exchange, and balance with the around ecosystem.

REFERENCES

- [1] R. E. M. Gregory and P. Asner, "Spectral and chemical analysis of tropical forests: Scaling from leaf to canopy levels," *Remote Sens. Environ.*, vol. 112, no. 10, pp. 3958–3970, 2008.
- [2] A. G. M. Schlemmer, J. Schepers, R. Ferguson, Y. Peng, J. Shanahan, and D. Rundquist, "Remote estimation of nitrogen and chlorophyll contents in maize at leaf and canopy levels," *Int. J. Appl. Earth Observ. Geoinf.*, vol. 25, pp. 47–54, 2013.
- [3] J. Eitel, L. Vierling, D. Long, and E. R. Hunt, "Early season remote sensing of wheat nitrogen status using a green scanning laser," *Agricultural Forest Meteorol.*, vol. 151, pp. 1338–1345, 2011.
- [4] K. Erdle, B. Mistele, and U. Schmidhalter, "Comparison of active and passive spectral sensors in discriminating biomass parameters and nitrogen status in wheat cultivars," *Field Crops Res.*, vol. 124, no. 1, pp. 74–84, 2011.
- [5] W. Wagner, M. Hollaus, C. Briese, and V. Ducic, "3D vegetation mapping using small-footprint full-waveform airborne laser scanners," *Int. J. Remote Sens.*, vol. 29, no. 5, pp. 1433–1452, 2008.
- [6] J. Eitel, L. A. Vierling, and D. S. Long, "Simultaneous measurements of plant structure and chlorophyll content in broadleaf saplings with a terrestrial laser scanner," *Remote Sens. Environ.*, vol. 114, no. 10, pp. 2229–2237, 2010.
- [7] Z. Zhang, C. Wang, H. Zhang, Y. Tang, and X. Liu, "Analysis of permafrost region coherence variation in the Qinghai–Tibet Plateau with a high-resolution TerraSAR-X image," *Remote Sens.*, vol. 10, no. 2, 2018, Art. no. 298.
- [8] F. Hosoi and K. Omasa, "Estimation of vertical plant area density profiles in a rice canopy at different growth stages by high-resolution portable scanning LiDAR with a lightweight mirror," *ISPRS J. Photogramm. Remote Sens.*, vol. 74, pp. 11–19, 2012.
- [9] T. Magney, S. A. Eusden, J. Eitel, A. Barry, J. Jingjue, and A. Lee, "Assessing leaf photoprotective mechanisms using terrestrial lidar: Towards mapping canopy photosynthetic performance in three dimensions," *New Phytologist*, vol. 201, no. 1, pp. 344–356, 2014.
- [10] X. Zhu, T. Wang, R. Darvishzadeh, A. K. Skidmore, and K. O. Niemann, "3D leaf water content mapping using terrestrial laser scanner backscatter intensity with radiometric correction," *ISPRS J. Photogramm. Remote Sens.*, vol. 110, pp. 14–23, 2015.
- [11] J. Eitel, T. Magney, L. Vierling, T. Brown, and D. Huggins, "LiDAR based biomass and crop nitrogen estimates for rapid, non-destructive assessment of wheat nitrogen status," *Field Crops Res.*, vol. 159, pp. 21–32, 2014.
- [12] K. B. Hans-Werner Olfs, F. Brentrup, J. Jasper, A. Link, and J. Lammel, "Soil- and plant-based nitrogen-fertilizer recommendations in arable farming," *J. Plant Nutrition Soil Sci.*, vol. 168, no. 4, pp. 414–431, 2005.
- [13] H. Yanbo, L. Chunning, J. Luping, L. Deyang, and Z. Xiyang, "Growth performance and nitrogen allocation within leaves of two poplar clones after exponential and conventional nitrogen applications," *Plant Physiol. Biochem.*, vol. 154, pp. 530–537, 2020.
- [14] R. Gaulton, F. M. Danson, F. A. Ramirez, and O. Gunawan, "The potential of dual-wavelength laser scanning for estimating vegetation moisture content," *Remote Sens. Environ.*, vol. 132, pp. 32–39, 2013.
- [15] F. Danson *et al.*, "Developing a dual-wavelength full-waveform terrestrial laser scanner to characterize forest canopy structure," *Agricultural Forest Meteorol.*, vol. 198, pp. 7–14, 2014.
- [16] K. Benjamin *et al.*, "Fusion of imaging spectrometer and LiDAR data over combined radiative transfer models for forest canopy characterization," *Remote Sens. Environ.*, vol. 106, pp. 449–459, 2007.
- [17] O. Nevalainen, T. Hakala, J. Suomalainen, and S. Kaasalainen, "Nitrogen concentration estimation with hyperspectral LiDAR," *ISPRS Ann. Photogramm. Remote Sens. Spatial Inf. Sci.*, vol. II-5/W2, pp. 205–210, 2013.
- [18] J. Eitel, T. Magney, L. Vierling, and D. Günter, "Assessment of crop foliar nitrogen using a novel dual-wavelength laser system and implications for conducting laser-based plant physiology," *ISPRS J. Photogramm. Remote Sens.*, vol. 97, pp. 229–240, 2014.
- [19] L. Du *et al.*, "Estimation of rice leaf nitrogen contents based on hyperspectral LiDAR," *Int. J. Appl. Earth Observ. Geoinf.*, vol. 44, pp. 136–143, 2016.
- [20] I. H. Woodhouse *et al.*, "A multispectral canopy LiDAR demonstrator project," *IEEE Geosci. Remote Sens. Lett.*, vol. 8, no. 5, pp. 839–843, Sep. 2011.
- [21] S. Kaasalainen, T. Lindroos, and J. Hyppä, "Toward hyperspectral lidar: Measurement of spectral backscatter intensity with a supercontinuum laser source," *IEEE Geosci. Remote Sens. Lett.*, vol. 4, no. 4, pp. 211–215, 2007.
- [22] J. U. H. Eitel *et al.*, "Beyond 3-D: The new spectrum of lidar applications for earth and ecological sciences," *Remote Sens. Environ.*, vol. 186, pp. 372–392, 2016.
- [23] T. Hakala, S. Kaasalainen, and Y. Chen, "Full waveform hyperspectral LiDAR for terrestrial laser scanning," *Opt. Express*, vol. 20, no. 7, pp. 7119–7127, 2012.
- [24] W. Li, Z. Niu, G. Sun, S. Gao, and M. Wu, "Deriving backscatter reflective factors from 32-channel full-waveform LiDAR data for the estimation of leaf biochemical contents," *Opt. Express*, vol. 24, no. 5, pp. 4771–4785, 2016.
- [25] O. Nevalainen *et al.*, "Fast and nondestructive method for leaf level chlorophyll estimation using hyperspectral LiDAR," *Agricultural Forest Meteorol.*, vol. 198, pp. 250–258, 2014.
- [26] L. Du, W. Gong, and J. Yang, "Application of spectral indices and reflectance spectrum on leaf nitrogen content analysis derived from hyperspectral LiDAR data," *Opt. Laser Technol.*, vol. 107, pp. 372–379, 2018.
- [27] C. Daughtry, C. Walthall, M. Kim, E. B. De Colstoun, and J. McMurtrey III, "Estimating corn leaf chlorophyll concentration from leaf and canopy reflectance," *Remote Sens. Environ.*, vol. 74, pp. 229–239, 2000.
- [28] P. S. Thenkabail, R. B. Smith, and E. De Pauw, "Hyperspectral vegetation indices and their relationships with agricultural crop characteristics," *Remote Sens. Environ.*, vol. 71, pp. 158–182, 2000.
- [29] A. A. Gitelson, A. Vina, V. Ciganda, D. C. Rundquist, and T. J. Arkebauer, "Remote estimation of canopy chlorophyll content in crops," *Geophys. Res. Lett.*, vol. 32, no. 8, pp. 1–4, 2005.
- [30] P. S. A. Beck, C. Atzberger, K. A. Hogda, B. Johansen, and A. K. Skidmore, "Improved monitoring of vegetation dynamics at very high latitudes: A new method using MODIS NDVI," *Remote Sens. Environ.*, vol. 100, pp. 321–334, 2006.
- [31] R. S. Lunetta, J. F. Knight, J. Ediriyickrema, J. G. Lyon, and L. D. Worthy, "Land-cover change detection using multi-temporal MODIS NDVI data," *Remote Sens. Environ.*, vol. 105, pp. 142–154, 2006.
- [32] P. B. M. S. Mkhabela, S. Raj, S. Wang, and Y. Yang, "Crop yield forecasting on the Canadian Prairies using MODIS NDVI data," *Agricultural Forest Meteorol.*, vol. 151, no. 3, pp. 385–393, 2011.
- [33] C. D. Elvidge and Z. Chen, "Comparison of broad-band and narrow-band red and near-infrared vegetation indices," *Remote Sens. Environ.*, vol. 54, pp. 38–48, 1995.
- [34] E. F. M. Vincini and P. D'Alessio, "A broad-band leaf chlorophyll vegetation index at the canopy scale," *Precis. Agriculture*, vol. 9, no. 5, pp. 303–319, 2008.
- [35] B. Wang, L. Han, C. Chen, and Z. Wang, "The complete chloroplast genome sequence of Dieffenbachia seguine (Araceae)," *Mitochondrial DNA*, vol. 27, no. 4, pp. 2913–2914, 2015.
- [36] E. Raymond Hunt and C. S. Daughtry, "Chlorophyll meter calibrations for chlorophyll content using measured and simulated leaf transmittances," *Agronomy J.*, vol. 106, no. 3, pp. 931–939, 2014.
- [37] G. Wang, K. Bronson, K. Thorp, J. Mon, and M. Badaruddin, "Multiple leaf measurements improve effectiveness of chlorophyllmeter for durum wheat nitrogen management," *Crop Sci.*, vol. 54, pp. 817–826, 2014.
- [38] S. Peng, F. Garcia, R. Laza, A. Sanico, R. Visperas, and K. Cassman, "Increased N-use efficiency using a chlorophyll meter onhigh-yielding irrigated rice," *Field Crops Res.*, vol. 47, pp. 243–252, 1996.
- [39] J. Naus, J. Prokopova, J. Rebicek, and M. Spundova, "SPAD chlorophyll meter reading can be pronouncedly affected by chloroplastmovement," *Photosynthesis Res.*, vol. 105, pp. 265–271, 2010.
- [40] D. Xiong *et al.*, "SPAD-based leaf nitrogen estimation is impacted by environmental factors and crop leaf characteristics," *Sci. Rep.*, vol. 5, pp. 1–12, 2015.
- [41] J. Yoonch, "Multiple predicting K-fold cross-validation for model selection," *J. Nonparametric Statist.*, vol. 30, pp. 197–215, 2018.

- [42] W. Tzu-Tsung, "Performance evaluation of classification algorithms by k-fold and leave-one-out cross validation," *Pattern Recognit.*, vol. 48, no. 9, pp. 2839–2846, 2015.
- [43] B. Yegnanarayana, *Artificial Neural Networks*. PHI Learning Pvt. Ltd., 2009, pp. 201–232.
- [44] C. Zhang *et al.*, "Radiometric calibration for incidence angle, range and sub-footprint effects on hyperspectral LiDAR backscatter intensity," *Remote Sens.*, vol. 12, 2020, Art. no. 2855.
- [45] X. Li, L. Ma, and L. J. Xu, "Empirical modeling for non-Lambertian reflectance based on full-waveform laser detection," *Opt. Eng.*, vol. 52, 2013, Art. no. 116110.
- [46] K. Tan and X. J. Cheng, "Specular reflection effects elimination in terrestrial laser scanning intensity data using phong model," *Remote Sens.*, vol. 9, 2017, Art. no. 853.
- [47] S. Kaasalainen, M. Akerblom, O. Nevalainen, T. Hakala, and M. Kaasalainen, "Uncertainty in multispectral lidar signals caused by incidence angle effects," *Interface Focus*, vol. 8, 2018, Art. no. 20170033.
- [48] W. Wagner, "Radiometric calibration of small-footprint full-waveform airborne laser scanner measurements: Basic physical concepts," *ISPRS J. Photogramm. Remote Sens.*, vol. 65, pp. 505–513, 2010.
- [49] S. S. Chen Biwu *et al.*, "Hyperspectral lidar point cloud segmentation based on geometric and spectral information," *Opt. Express*, vol. 27, no. 17, pp. 24043–24059, 2019.
- [50] F. Humair, A. Abellan, D. Carrea, B. Matasci, J.-L. Epard, and M. Jaboyedoff, "Geological layers detection and characterisation using high resolution 3D point clouds: Example of a box-fold in the Swiss Jura Mountains," *Eur. J. Remote Sens.*, vol. 48, no. 1, pp. 541–568, 2015.
- [51] D. Carrea, A. Abellan, F. Humair, B. Matasci, M.-H. Derron, and M. Jaboyedoff, "Correction of terrestrial LiDAR intensity channel using Oren-Nayar reflectance model: An application to lithological differentiation," *ISPRS J. Photogramm. Remote Sens.*, vol. 113, pp. 17–29, 2016.
- [52] P. Hu *et al.*, "Analyzing the angle effect of leaf reflectance measured by indoor hyperspectral light detection and ranging (LiDAR)," *Remote Sens.*, vol. 12, no. 6, 2020, Art. no. 919.
- [53] M. S. Kim, C. Daughtry, E. Chappelle, J. McMurtrey, and C. Walthall, "The use of high spectral resolution bands for estimating absorbed photosynthetically active radiation (A par)," 1994.
- [54] N. H. Broge and E. Leblanc, "Comparing prediction power and stability of broadband and hyperspectral vegetation indices for estimation of green leaf area index and canopy chlorophyll density," *Remote Sens. Environ.*, vol. 76, pp. 156–172, 2001.
- [55] D. Haboudane, J. R. Miller, N. Tremblay, P. J. Zarco-Tejada, and L. Dextraze, "Integrated narrow-band vegetation indices for prediction of crop chlorophyll content for application to precision agriculture," *Remote Sens. Environ.*, vol. 81, pp. 416–426, 2002.
- [56] R. Merton and J. Huntington, "Early simulation results of the ARIES-1 satellite sensor for multi-temporal vegetation research derived from AVIRIS," in *Proc. 8th Annu. JPL Airborne Earth Sci. Workshop*, 1999, pp. 8–14.
- [57] J. Delegido, L. Alonso, G. González, and J. Moreno, "Estimating chlorophyll content of crops from hyperspectral data using a normalized area over reflectance curve (NAOC)," *Int. J. Appl. Earth Observ. Geoinf.*, vol. 12, pp. 165–174, 2010.
- [58] M. Reyniers, D. J. Walvoort, and J. De Baerdemaeker, "A linear model to predict with a multi-spectral radiometer the amount of nitrogen in winter wheat," *Int. J. Remote Sens.*, vol. 27, no. 19, pp. 4159–4179, 2006.
- [59] N. S. Goel and W. Qin, "Influences of canopy architecture on relationships between various vegetation indices and LAI and FPAR: A computer simulation," *Remote Sens. Rev.*, vol. 10, no. 4, pp. 309–347, 1994.
- [60] R. Huang and M. He, "Band selection based on feature weighting for classification of hyperspectral data," *IEEE Geosci. Remote Sens. Lett.*, vol. 2, no. 2, pp. 156–159, Apr. 2005.
- [61] R. Dickson, "Carbon and nitrogen allocation in trees," *Annales des Sciences Forestières*, vol. 46, pp. 631s–647s, 1989.
- [62] T. Takashima, K. Hikosaka, and T. Hirose, "Photosynthesis or persistence: Nitrogen allocation in leaves of evergreen and deciduous quercus species," *Plant, Cell Environ.*, vol. 27, pp. 1047–1054, 2004.
- [63] D. A. Sims and J. Gamon, "Relationship between leaf pigment content and spectral reflectance across of a wide range of species, leaf structure and development stages," *Remote Sens. Environ.*, vol. 81, pp. 337–354, 2002.
- [64] A. Gitelson, G. Keydan, and M. Merzlyak, "Three-band model for invasive estimation of chlorophyll, carotenoids and anthocyanin content in higher plant leaves," *Geophys. Res. Lett.*, vol. 33, pp. 431–433, 2006.
- [65] S. Xiao, K. Bi, S. Gao, C. Zhang, N. Huang, and Z. Niu, "Estimating vertical chlorophyll concentrations in maize in different health states using hyperspectral LiDAR," *IEEE Trans. Geosci. Remote Sens.*, vol. 58, no. 11, pp. 8125–8133, Nov. 2020.
- [66] J. Yang *et al.*, "Assessing different regression algorithms for paddy rice leaf nitrogen concentration estimations from the first-derivative fluorescence spectrum," *Opt. Express*, vol. 28, no. 13, pp. 18728–11874, 2020.
- [67] S. Kaasalainen, T. Hakala, O. Nevalainen, E. Puttonen, and K. Anttila, "Hyperspectral lidar in non-destructive 4D monitoring of climate variables," *Int. Arch. Photogramm., Remote Sens., Spatial Inf. Sci.*, vol. 40, pp. 109–111, 2014.
- [68] L. Du, J. Yang, J. Sun, S. Shi, and W. Gong, "Leaf biochemistry parameters estimation of vegetation using the appropriate inversion strategy," *Frontiers Plant Sci.*, vol. 11, 2020, Art. no. 533.
- [69] S. Jacquemoud *et al.*, "PROSPECT+SAIL models: A review of use for vegetation characterization," *Remote Sens. Environ.*, vol. 113, pp. S56–S66, 2009.
- [70] J. P. G. Etchegorry *et al.*, "Discrete anisotropic radiative transfer (DART 5) for modeling airborne and satellite spectroradiometer and LiDAR acquisitions of natural and urban landscapes," *Remote Sens.*, vol. 7, pp. 1667–1170, 2015.
- [71] H. Huang, W. Qin, and Q. Liu, "RAPID: A radiosity applicable to porous individual objects for directional reflectance over complex vegetated scenes," *Remote Sens. Environ.*, vol. 132, pp. 221–237, 2013.
- [72] N. Wenge, L. B. David, and D. Ralph, "Modeling lidar waveforms in heterogeneous and discrete canopies," *IEEE Trans. Geosci. Remote Sens.*, vol. 39, no. 9, pp. 1943–1958, Sep. 2001.
- [73] Q. X. Yi, J. F. Huang, F. M. Wang, X. Z. Wang, and Z. Y. Liu, "Monitoring rice nitrogen status using hyperspectral reflectance and artificial neural network," *Environ. Sci. Technol.*, vol. 41, no. 19, pp. 6770–6775, 2007.
- [74] E. W. Chappelle, M. S. Kim, and J. E. McMurtrey III, "Ratio analysis of reflectance spectra (RARS): An algorithm for the remote estimation of the concentrations of chlorophyll A, chlorophyll B, and carotenoids in soybean leaves," *Remote Sens. Environ.*, vol. 39, pp. 239–247, 1992.
- [75] S. Shi, S. L. Song, W. Gong, L. Du, B. Zhu, and X. Huang, "Improving backscatter intensity calibration for multispectral LiDAR," *IEEE Geosci. Remote Sens. Lett.*, vol. 12, no. 7, pp. 1421–1425, Jul. 2015.
- [76] J. Uddling, J. Gelang-Alfredsson, K. Piikki, and H. Pleijel, "Evaluating the relationship between leaf chlorophyll concentration and SPAD-502 chlorophyll meter readings," *Photosynthesis Res.*, vol. 91, pp. 37–46, 2007.
- [77] C. Barutcular *et al.*, "Evaluation of SPAD chlorophyll in spring wheat genotypes under different environments," *Fresenius Environ. Bull.*, vol. 25, pp. 1258–1266, 2016.



Lin Du received the Ph.D. degree in condensed matter physics from Wuhan University, Wuhan, China, in 2017.

He is currently an Associate Professor with the School of Geography and Information Engineering, China University of Geosciences, Wuhan, China. His research interests include hyperspectral LiDAR detection and its application in vegetation monitoring, especially in the 3-D biochemical parameter reversion and reconstruction in canopy level.



Zhili Jin was born in Henan, China, in 2000. He is currently working toward the bachelor's degree in surveying and mapping with the School of Geoscience and Info-Physics, Central South University, Changsha, China.

His research interests include LiDAR remote sensing, point cloud processing, and application.



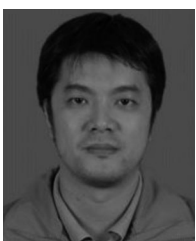
Bowen Chen received the B.E. degree in surveying and mapping engineering from Henan Polytechnic University, Jiaozuo, China, in 2017. He is currently working toward the Ph.D. degree in photogrammetry and remote sensing with the State Key Laboratory of Information Engineering in Surveying, Mapping and Remote Sensing, Wuhan University, Wuhan, China.

His research interests include true-color 3-D imaging using hyperspectral light detection and ranging data.



Biwu Chen received the B.S. degree in remote sensing science and technology in 2015 from the School of Remote Sensing and Information Engineering, Wuhan University, Wuhan, China, where he is currently working toward the Ph.D. degree in photogrammetry and remote sensing with the State Key Laboratory of Information Engineering in Surveying, Mapping and Remote Sensing.

His research interests include hyperspectral lidar data processing, point cloud classification, and segmentation.



Wei Gao received the Ph.D. degree in cartography and geographical information engineering from the China University of Geosciences, Wuhan, China, in 2010.

He is currently an Associate Professor with the School of Geography and Information Engineering, China University of Geosciences. His research interests include eco-environment and vegetation remote sensing and monitoring.



Jian Yang received the Ph.D. degree in photogrammetry and remote sensing from Wuhan University, Wuhan, China, in 2017.

He is currently an Associate Professor with the School of Geography and Information Engineering, China University of Geosciences, Wuhan, China. His research interests include radiation transfer model, light detection, laser-induced fluorescence technology, and its application in quantitative monitoring.



Shuo Shi (Member, IEEE) received the Ph.D. degree in photogrammetry and remote sensing from Wuhan University, Wuhan, China, in 2015.

He is currently an Associate Professor with the State Key Laboratory of Information Engineering in Surveying, Mapping and Remote Sensing, Wuhan University. He has been supported the “Wuhan Morning Light Plan of Youth Science and Technology.” He has authored more than 30 peer-reviewed research papers. His research interests include hyperspectral lidar, fluorescence lidar, true-color imaging, target classification, and vegetation quantitative remote sensing.



Shalei Song received the B.S. degree in geography information system and the Ph.D. degree in remote sensing from Wuhan University, Wuhan, China, in 2004 and 2010, respectively.

Since 2013, he has been a Professor with the Wuhan Institute of Physics and Mathematics, Chinese Academy of Sciences, Wuhan, China. His research interests include multispectral lidar development for earth observation and investigation of new optical remote sensing methods for vegetation and atmosphere detection.



Mengmeng Wang received the B.S. degree in geoscience information system from the Hefei University of Technology, Hefei, China, in 2012, and the Ph.D. degree in photogrammetry and remote sensing from the Institute of Remote Sensing and Digital Earth, Chinese Academy of Sciences, Beijing, China, in 2017.

He is currently a Lecturer with the School of Geography and Information Engineering, China University of Geosciences, Wuhan, China. His main research interests include thermal infrared quantitative remote sensing and their applications on nature hazards and agriculture.



Wei Gong received the B.S. degree in photonics engineering from the Huazhong University of Science and Technology (HUST), Wuhan, China, in 1993, the M.S. degree in electronics from the Chinese Academy of Science, Lanzhou, China, in 1996, and the Ph.D. degree in physical electronics from HUST in 1999.

From 2002 to 2004, he served as an Assistant Professor with Hampton University, Hampton, VA, USA. He is currently a Professor with the Electronic Information School, Wuhan University, Wuhan, China. He is mainly engaged in teaching and research of new

lasers, optical technology, and its remote sensing applications, and has made achievements in atmospheric lidar and optical remote sensing. In recent years, he has more than 100 scientific papers accepted and published, 18 patents, and two books coauthored.



Wei Wang received the Ph.D. degree in photogrammetry and remote sensing from Wuhan University, Wuhan, China, in 2017.

He is currently an Associate Professor with the School of Geoscience and Info-Physics, Central South University, Changsha, China. His research interests include optical and laser remote sensing, remote sensing of atmospheric environment, and point cloud processing and application.